Catalysis Science & Technology

ROYAL SOCIETY OF CHEMISTRY

PAPER

View Article Online
View Journal | View Issue

Open Access Article. Published on 24 February 2023. Downloaded on 10/30/2025 4:25:35 AM.
This article is licensed under a Creative Commons Attribution 3.0 Unported Licence.

Check for updates

Cite this: *Catal. Sci. Technol.*, 2023, **13**, 2038

Co_3O_4/TiO_2 catalysts studied *in situ* during the preferential oxidation of carbon monoxide: the effect of different TiO_2 polymorphs†

Thulani M. Nyathi,[a] Mohamed I. Fadlalla,[a] Nico Fischer,[a] Andrew P. E. York,[b] Ezra J. Olivier,[c] Emma K. Gibson,[de] Peter P. Wells[efg] and Michael Claeys *[a]

Received 29th September 2022,
Accepted 23rd February 2023

DOI: 10.1039/d2cy01699k

rsc.li/catalysis

Co_3O_4 nanoparticles were supported on different TiO_2 polymorphs, namely, rutile, anatase, and a 15 : 85 mixture of rutile and anatase (also known as P25), *via* incipient wetness impregnation. The Co_3O_4/TiO_2 catalysts were evaluated in the preferential oxidation of CO (CO-PrOx) in a H_2-rich gas environment and characterised *in situ* using PXRD and magnetometry. Our results show that supporting Co_3O_4 on P25 resulted in better catalytic performance, that is, a higher maximum CO conversion to CO_2 of 72.7% at 200 °C was achieved than on rutile (60.7%) and anatase (51.5%). However, the degree of reduction (DoR) of Co_3O_4 to Co^0 was highest on P25 (91.9% at 450 °C), with no $CoTiO_3$ detected in the spent catalyst. The DoR of Co_3O_4 was lowest on anatase (76.4%), with the presence of Ti_xO_y-encapsulated CoO_x nanoparticles and bulk $CoTiO_3$ (13.8%) also confirmed in the spent catalyst. Relatively low amounts of $CoTiO_3$ (8.9%) were detected in the spent rutile-supported catalyst, while a higher DoR (85.9%) was reached under reaction conditions. The Co^0 nanoparticles formed on P25 and rutile existed in the fcc and hcp crystal phases, while only fcc Co^0 was detected on anatase. Furthermore, undesired CH_4 formation took place over the Co^0 present in the P25- and rutile-supported catalysts, while CH_4 was not formed over the Co^0 on anatase possibly due to encapsulation by Ti_xO_y species. For the first time, this study revealed the influence of different TiO_2 polymorphs (used as catalyst supports) on the chemical and crystal phase transformations of Co_3O_4, which in turn affect its activity and selectivity during CO-PrOx.

1. Introduction

Titanium(IV) oxide (or titania, TiO_2) is a highly versatile material with applications in the manufacture of paint, paper, and plastic products as a pigmentation agent.[1] It is also used by the cosmetics industry as a sun-blocking agent in sunscreen products.[2] Owing to its excellent capability to absorb sunlight, TiO_2 has found great use as a photocatalyst, for example, to produce carbon-free hydrogen (H_2) and oxygen (O_2) *via* water (H_2O) electrolysis.[3,4] In other catalysed reactions, TiO_2 is employed as a support material that anchors active nanoparticles to minimise their growth in size (*i.e.*, sintering) and loss of chemical phase (*e.g.*, *via* reduction or oxidation).[5–9]

Depending on the catalytic process, strong nanoparticle–support interactions (NPSI) may have a negative impact on the performance of the catalyst as the active phase can be lost through reacting with TiO_2 to form Ti-containing mixed metal oxides such as titanates.[6,7,9] For example, the formation of cobalt titanates (*e.g.*, $CoTiO_3$) has been observed in the Fischer–Tropsch synthesis (FTS) when operating Co/TiO_2 catalysts under high synthesis gas conversion environments because of the high $H_2O:H_2$ partial pressure ratios realised.[10–12] In other cases, the surface of TiO_2 can be partially reduced to form Ti_xO_y species that subsequently migrate and encapsulate the reduced Co particles due to the surface energy of TiO_2 (*e.g.*, anatase: 0.44 J m^{-2}) being lower than that of metallic Co (*e.g.*, face-centred cubic (fcc) Co^0: 2.6 J m^{-2}).[13–15] The encapsulation can also lead to the formation of cobalt titanates.[7,10,16]

[a] Catalysis Institute and c*change (DSI-NRF Centre of Excellence in Catalysis), Department of Chemical Engineering, University of Cape Town, Rondebosch 7701, South Africa. E-mail: michael.claeys@uct.ac.za
[b] Johnson Matthey Technology Centre, Sonning Common, Reading RG4 9NH, UK
[c] Centre for High Resolution Transmission Electron Microscopy, Physics Department, Nelson Mandela University, PO Box 77000, Gqeberha, 6031, South Africa
[d] School of Chemistry, Joseph Black Building, University of Glasgow, Glasgow G12 8QQ, UK
[e] UK Catalysis Hub, Research Complex at Harwell, Rutherford Appleton Laboratory, Harwell, Oxon, OX11 0FA, UK
[f] School of Chemistry, University of Southampton, University Road, Southampton SO17 1BJ, UK
[g] Diamond Light Source Ltd., Harwell Science and Innovation Campus, Chilton, Didcot OX11 0DE, UK

† Electronic supplementary information (ESI) available. See DOI: https://doi.org/10.1039/d2cy01699k

 This journal is © The Royal Society of Chemistry 2023

Open Access Article. Published on 24 February 2023. Downloaded on 10/30/2025 4:25:35 AM.
This article is licensed under a Creative Commons Attribution 3.0 Unported Licence.

There are three well reported crystal forms or polymorphs of TiO_2, namely, rutile, anatase, and brookite. Rutile is the most stable of all the three polymorphs and can be produced in pure bulk form typically at high temperatures (600–800 °C) from either anatase or brookite.[17] Rutile and anatase are the widely utilised forms of TiO_2 in the industries/fields mentioned earlier, and the application can either involve the pure form of one of the polymorphs or a mixture of both polymorphs. Owing to their different physical properties (such as surface area and porosity) and differences in the arrangement of atoms in their respective crystal lattices, the behaviours of rutile and anatase may also differ.[1,18]

For example, anatase is generally considered a better photocatalyst than rutile because of its greater charge transfer capability.[19,20] On the other hand, rutile-supported Co catalysts often exhibit a superior catalytic performance than that of their anatase-supported counterparts in the FTS.[21,22] The lower activity of anatase-supported Co catalysts may be caused by the encapsulation and/or loss of active Co *via* cobalt titanate formation, both of which are kinetically and thermodynamically more facile in H_2O–H_2 environments when anatase is used as the support.[10–12] However, some researchers have reported improved catalytic performance when a mixture of rutile and anatase is employed, which has given rise to the wide range of nano-sized rutile–anatase mixtures being applied in various catalytic processes in recent years.[4,21]

In this study, we have supported cobalt(II,III) oxide (Co_3O_4) nanoparticles *via* incipient wetness impregnation on rutile, anatase, and the commercially available mixture of rutile and anatase (at a 15 : 85 ratio) called "P25" (from Evonik Industries). The three supported catalysts were evaluated for activity, selectivity, and phase stability in the preferential oxidation of carbon monoxide (CO-PrOx) in a H_2-rich gas environment. CO-PrOx is an essential H_2 'clean-up' process that helps remove the trace amounts of CO (0.5–2%) that adsorb and deactivate the Pt-containing anode catalyst of proton-exchange membrane fuel cells (PEMFCs).[23,24] Co_3O_4 is generally regarded as the most active phase of Co in the context of CO oxidation and CO-PrOx, which take place *via* the Mars–van Krevelen (MvK) mechanism.[25,26] Therefore, the loss of this oxide phase through reduction by the abundant H_2 (40–75%) decreases the carbon dioxide (CO_2) yield and selectivity in CO-PrOx. Moreover, the ultimate formation of Co^0 changes the conversion pathway of CO from oxidation to hydrogenation, which produces undesired methane (CH_4).[27–33]

Our previous study reported the effect of different support materials (*viz.*, CeO_2, ZrO_2, SiC, SiO_2, and Al_2O_3) on the performance and phase stability of Co_3O_4 nanoparticles during CO-PrOx.[32] More specifically, we proposed that weak NPSI (*e.g.*, in Co_3O_4/ZrO_2) allow for high CO_2 yields to be achieved *via* the MvK mechanism, which relies on the high surface reducibility (and re-oxidation) of the nanoparticles. However, the weak NPSI do not help stabilise the Co_3O_4 phase against surface and bulk reduction as Co^0 (and associated CH_4) is formed at relatively low temperatures. On the other hand, strong NPSI (*e.g.*, in Co_3O_4/Al_2O_3) helped stabilise the cobalt oxide phase and consequently limited CH_4 formation. However, we further showed that a less reducible catalyst is less active for CO oxidation because the MvK cycle becomes kinetically hindered.

To the best of our knowledge, there has not been a study reporting the effect of different TiO_2 polymorphs on the catalytic performance and phase stability of Co-based catalysts in the CO-PrOx reaction. Therefore, our current work involves the performance evaluation of Co_3O_4/TiO_2 catalysts (where TiO_2 = P25, rutile, or anatase) coupled with their *in situ* characterisation using powder X-ray diffraction (PXRD)[34–36] and magnetometry[36,37] during CO-PrOx. For the first time, we report a dependence of the catalytic performance of Co_3O_4 on the polymorph of TiO_2 used as the support. Furthermore, our *in situ* studies showed that certain chemical and crystallographic phase changes of Co_3O_4 (leading to CoO, $CoTiO_3$, fcc and/or hcp (hexagonal close-packed) Co^0) may also be dependent on the type of TiO_2 polymorph.

2. Experimental

2.1. Catalyst preparation

In the subsequent sections of the paper, the bare TiO_2 supports used are referred to as "P25", "rutile", and "anatase", while the Co_3O_4-loaded supports are referred to as "Co_3O_4/P25", "Co_3O_4/rutile", and "Co_3O_4/anatase".

The supported catalysts for this study were prepared *via* the incipient wetness impregnation of pre-calcined (300 °C) P25 (99.5% purity, Evonik Industries), rutile (99.5% purity, Merck), and anatase (99.7% purity, Merck) with an aqueous solution containing 1.2 g of $Co(NO_3)_2{\cdot}6H_2O$ (reagent grade 98% purity, Merck) for every 1 mL of deionised water. The impregnated supports were dried overnight at 60 °C under a flow of nitrogen (N_2, 50 mL(NTP) min^{-1}) and annealed for 60 min at 350 °C (heating rate: 2 °C min^{-1}) under the same gas flow at atmospheric pressure[38] in a glass tube (I.D.: 15 mm, length: 240 mm; Lasec SA). In the case of rutile, two impregnation steps were conducted to achieve the targeted Co_3O_4 loading of 10 wt% as this support had a low pore volume of 0.12 cm^3 g^{-1} (Table 1). The calcined material obtained after the first impregnation was used for the second impregnation.

The bare support materials as well as the fresh and spent TiO_2-supported Co_3O_4 catalysts were characterised *ex situ* using PXRD, scanning transmission electron microscopy coupled with electron energy loss spectroscopy (STEM-EELS), N_2 physisorption, inductively coupled plasma-optical emission spectroscopy (ICP-OES), and X-ray absorption spectroscopy (XAS). The details pertaining to these *ex situ* techniques can be found under the section "*ex situ* catalyst characterisation" in the ESI.†

Open Access Article. Published on 24 February 2023. Downloaded on 10/30/2025 4:25:35 AM.
This article is licensed under a Creative Commons Attribution 3.0 Unported Licence.

Table 1 *Ex situ* characterisation results for the fresh supported catalysts

Sample name	d_{PXRD}[a] (nm)	$d_{STEM,v}$[b] (nm)	$d_{STEM,n}$[c] (nm)	MSSA[d] (m^2 g^{-1})	v_{pore}[d] (cm^3 g^{-1})	Relative fraction of Co_3O_4[a] (wt%)	Co_3O_4 loading[e] (wt%)
Co_3O_4/P25	11.8 ± 0.3	14.2 ± 4.6	9.9 ± 3.7	37.0 (48.7)	0.19 (0.21)	10.3 ± 0.3	9.4
Co_3O_4/rutile	14.7 ± 0.3	15.5 ± 3.8	13.0 ± 3.3	23.7 (26.6)	0.08 (0.12)	10.3 ± 0.5	9.8
Co_3O_4/anatase	9.8 ± 0.2	16.6 ± 3.9	13.3 ± 3.9	73.5 (97.6)	0.23 (0.28)	8.5 ± 0.3	9.9

[a] Average volume-based crystallite size and relative weight fraction (with associated errors) of Co_3O_4. [b] Average volume-based particle size and standard deviation. [c] Average number-based particle size and standard deviation. [d] Values in parentheses are for the corresponding bare support. [e] Calculated based on the concentration of Co determined using ICP-OES.

2.2. *In situ* catalyst characterisation and evaluation

2.2.1. Reduction studies. The reduction of the bare supports and supported Co_3O_4 catalysts (*ca.* 0.012 g each) was performed at atmospheric pressure under a gas flow of 50% H_2 in N_2 (1.2 mL(NTP) min^{-1}) in an in-house developed PXRD capillary-based reaction cell.[34–36] Reduction studies were also performed *via* conventional H_2 temperature-programmed reduction (H_2-TPR) under a flow of 5% H_2 in Ar (50 mL(NTP) min^{-1}) at atmospheric pressure using a sample of approximately 0.1 g. The experimental procedures for the PXRD-based reduction and H_2-TPR studies, as well as the details for the data analysis can be found under the section "*in situ* catalyst characterisation" in the ESI.†

2.2.2. Catalyst evaluation during CO-PrOx. The bare supports and prepared catalysts were evaluated under model/dry CO-PrOx conditions (feed composition: 1% CO, 1% O_2, 50% H_2, and 48% N_2) at atmospheric pressure in the PXRD reaction cell mentioned earlier and in an in-house developed *in situ* sample magnetometer.[36,37] We note that the evaluation of the bare supports did not involve *in situ* characterisation as the supports were not expected to undergo (bulk) phase changes and are not ferromagnetic (also see sections 3.2.1. and 3.3.). Furthermore, the reaction gas feed did not contain H_2O and CO_2 as the effects of these gases have been reported in our previous publications.[31,32] The procedures followed for analysing the data obtained from the *in situ* techniques are detailed under the section "*in situ* catalyst characterisation" in the ESI.†

The magnetometer enables the detection of Co^0 (with no distinction between fcc and hcp Co^0) as it is the only ferromagnetic Co-based phase[39] among those that can be formed in the current study (*e.g.*, Co_3O_4, CoO, and $CoTiO_3$). However, the magnetometer is highly sensitive as very small amounts of Co^0 (*ca.* 0.23 mg, which is equivalent to 0.1 wt% in this study) can be detected,[30] while PXRD requires relative amounts of Co^0 (and of the other phases, *viz.*, Co_3O_4, CoO, and $CoTiO_3$) that are above 2–3 wt% for adequate detection.

The PXRD capillary reactor was loaded with approximately 0.012 g of catalyst each time, and while the magnetometry reactor was loaded with approximately 0.26 g. The reactors were heated from 50 to 450 °C at a rate of 1 °C min^{-1} while holding the temperature at every 25 °C for 60 min. The reaction feed was flowed at 1.2 mL(NTP) min^{-1} in the PXRD-based experiments and 25 mL(NTP) min^{-1} in the magnetometry-based experiments to achieve a gas-hourly space velocity (GHSV) of 60 000 mL(NTP) $g_{Co_3O_4}^{-1}$ h^{-1}, which is based on the Co_3O_4 loadings determined using ICP-OES (Table 1).

The reactor effluent gas from the CO-PrOx experiments was sampled on-line every 5 min using a Varian CP-4900 micro-GC (Agilent) fitted with thermal conductivity detectors for detecting CO, O_2, H_2, CO_2, CH_4, and N_2 in three different columns (see Table S1† for the identity of the columns and full set of parameters applied to achieve gas separation). The chromatographic analysis was operated using the Varian Galaxie Chromatography Data System (version 1.9.3.2). The relevant peak areas in each chromatogram were used to calculate the volumetric flow rates of each eluting gas using eqn (S1) and (S2).† The volumetric flow rates were subsequently used to calculate normalised gas outlet flow rates (eqn (S3)†), conversions/yields (eqn (S4) and (S5)†), and selectivities (eqn (S6)†). The formation of H_2O was inferred based on the results obtained using the abovementioned equations because H_2O could not be analysed in the micro-GC due to its prior condensation in a cold trapping vessel.

3. Results and discussion

3.1. *Ex situ* characterisation of fresh catalysts

Various *ex situ* characterisation techniques (*viz.*, PXRD, STEM-EELS, N_2 physisorption, and ICP-OES) were employed to determine the physicochemical properties of the bare supports and fresh supported Co_3O_4 catalysts. As mentioned earlier, the support material "P25" contains the rutile and anatase polymorphs at a 15 : 85 ratio, which was confirmed using Rietveld refinement in the TOPAS 5.0 software package[40] (see results in Fig. S3 and Table S3†). Additionally, this composition is qualitatively shown in the STEM-EELS Ti map of the bare P25 support (Fig. S4†), where the method ELNES (energy loss near edge structure) was used to distinguish the areas with rutile from those with anatase.

The diffraction patterns of the fresh catalysts are shown in Fig. 1 and those of the bare supports can be found in Fig. S5.† Despite the crystalline nature of the three supports used, most of the reflections from the Co_3O_4 phase are visible in the diffraction patterns shown in Fig. 1(b) and do not overlap with those from the support materials. The presence of $CoTiO_3$ was also considered (either

Open Access Article. Published on 24 February 2023. Downloaded on 10/30/2025 4:25:35 AM.
This article is licensed under a Creative Commons Attribution 3.0 Unported Licence.

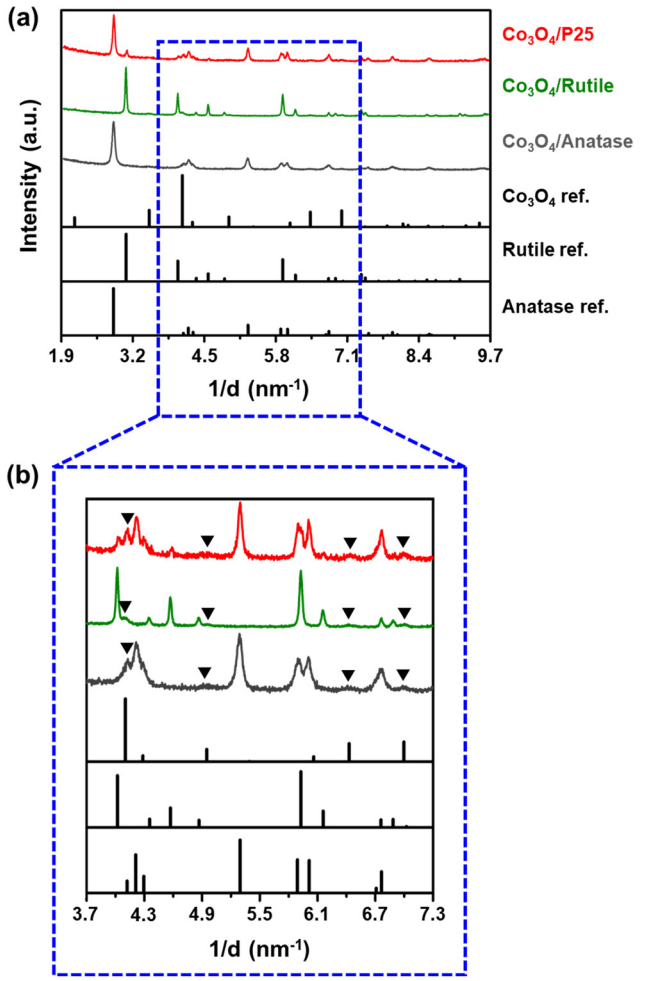

Fig. 1 (a) PXRD patterns (radiation source: Co Kα1 = 0.178897 nm) of the fresh supported catalysts and the reference reflection lines of Co_3O_4, rutile, and anatase as recorded in the ICDD PDF-2 database (see Table S2† for their PDF entry numbers). (b) Magnified short 1/*d* range of the recorded PXRD patterns for clarity of the Co_3O_4 reflections. The black triangles indicate the identified Co_3O_4 reflections in each diffraction pattern.

with a cubic or rhombohedral crystal structure) but no reflections from this phase can be observed in the acquired diffraction patterns (Fig. S6†). Based on Rietveld refinement, the average volume-based crystallite sizes of Co_3O_4 in the P25-, rutile-, and anatase-supported catalysts are 11.8 ± 0.3 nm, 14.7 ± 0.3 nm, and 9.8 ± 0.2 nm, respectively, while the relative weight fractions of Co_3O_4 in each catalyst are 10.3 ± 0.3 wt%, 10.3 ± 0.5 wt%, and 8.5 ± 0.3 wt%, respectively. It is worth noting that the relative weight fractions of Co_3O_4 for the P25- and rutile-supported catalysts are close to 10 wt%, which is the targeted loading in this study. The low Co_3O_4 weight fraction for the anatase-supported catalyst is likely a result of the excessive overlap of the Co_3O_4 and anatase reflections. This excessive overlap causes the Co_3O_4 reflections to be less visible, leading to a lower Co_3O_4 weight fraction being estimated using Rietveld refinement. Other Rietveld refinement results, based on the diffraction patterns in Fig. 1 (*e.g.*, the fitted phases and R_{wp} values), can be found in Fig. S7 and Table S4.†

Bright-field STEM micrographs, corresponding Co maps (generated based on the Co L-edge), and derived number-based size distributions for each catalyst are shown in Fig. 2. The Co maps generally show a good distribution of the Co_3O_4 particles over the various supports, but with some clustered particles also identifiable. For particle size analysis, only the Co-bearing entities that appear as single particles were measured to obtain number-based size distributions as well as average number- and volume-based particle sizes (see eqn (S8)–(S11)† and the results in Table 1). The average Co_3O_4 particles sizes (on a number and volume basis) vary within a narrow range of approximately 3 nm among the three catalysts prepared, and the STEM-derived volume-based sizes are larger than the PXRD-derived volume-based sizes. This could indicate the presence of smaller Co_3O_4 crystalline domains (detected using PXRD) that constitute the larger particles identified using STEM-EELS.[41]

The BET (Brunauer–Emmett–Teller) surface areas and BJH (Barrett–Joyner–Halenda) pore volumes of the bare and Co_3O_4-loaded supports are shown in Table 1. The surface areas and pore volumes of the supports decrease after supporting Co_3O_4, which is often observed with supported catalysts prepared using incipient wetness impregnation (as in the current study).[32,42] The decrease in the pore volume may indicate the presence of (most of the) Co_3O_4 particles in the pores of each support. The ICP-OES-derived Co loading (in the form of Co_3O_4) in each catalyst is close to the targeted 10 wt% loading and in agreement with the Co_3O_4 relative weight fractions calculated using Rietveld refinement, especially for Co_3O_4/P25 and Co_3O_4/rutile (Table 1).

3.2. *In situ* reduction studies

3.2.1. PXRD-based reduction. The reducibility of the fresh TiO_2-supported catalysts was studied under a flow of 50% H_2 in N_2 at atmospheric pressure between 50 and 450 °C. This was coupled with *in situ* PXRD measurements taken every 5 min (or every 5 °C) throughout each experiment. The recorded diffraction patterns are plotted in Fig. 3(a) and 4(a) as a function of temperature but showing the on-top view of the diffractions patterns to allow for better visualisation of the appearing and disappearing reflections. Rietveld refinement was applied to calculate the relative weight fraction (Fig. 3(b) and 4(b)) and average crystallite size (Fig. 3(c) and 4(c)) of each Co-based phase formed. The weight fractions reported are on a Co basis, that is, the weight fraction of the support is not reported in each case.

It can be observed that the Co_3O_4 crystallites supported on P25 and rutile reduce to CoO at 205 °C, while on anatase, this reduction step is first observed at 230 °C. Based on Rietveld refinement, the starting Co_3O_4 crystallites supported on anatase have a smaller size than those supported on rutile

Open Access Article. Published on 24 February 2023. Downloaded on 10/30/2025 4:25:35 AM.
This article is licensed under a Creative Commons Attribution 3.0 Unported Licence.

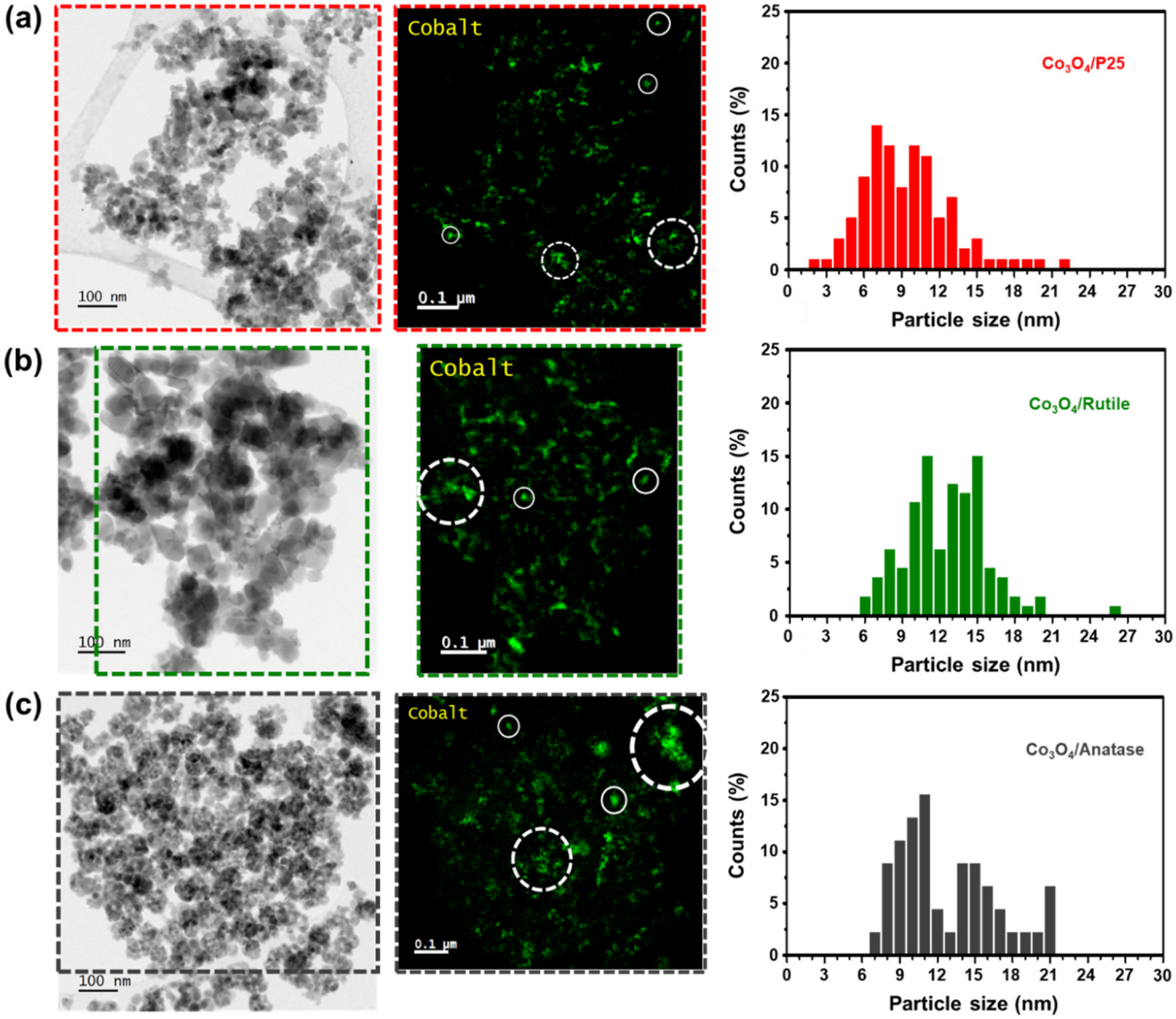

Fig. 2 (Left) Selected bright-field STEM micrographs of the fresh catalysts (a) Co_3O_4/P25, (b) Co_3O_4/rutile, and (c) Co_3O_4/anatase. (Middle) Corresponding STEM-EELS Co maps (generated based on the Co L-edge) showing the location of Co-bearing particles/clusters. (Right) Derived number-based size distributions. The solid white circles in the Co maps indicate the "single" Co-bearing particles and the dashed white circles indicate "clusters" of Co-bearing particles.

and P25 (Table 1 as well as Fig. 3(c) and 4(c)), which might explain their delayed reduction.[43–45] This may be further enhanced by the existence of stronger NPSI between Co_3O_4 and anatase.[7,10,16,21,22] In general, the CoO crystallites formed are either similar (in the case of Co_3O_4/anatase) or smaller than the starting Co_3O_4 crystallites (as in the case of Co_3O_4/P25 and Co_3O_4/rutile), which indicates minimal or no sintering. The CoO crystallites supported on rutile reduce at 285 °C to fcc Co^0 only, while the CoO crystallites on P25 and anatase reduce later at 305 °C to fcc and hcp Co^0 (also see Fig. S8† for further evidence of hcp Co^0 formation).

The formation of fcc Co^0 only or both fcc and hcp Co^0 during the reduction of cobalt oxides is common and may be influenced by the starting crystallite size (or size distribution) of cobalt oxide among other things.[46] Pure hcp Co^0 is thermodynamically stable above 20 nm, while fcc Co^0 is stable below 20 nm.[47,48] In this study, the metallic crystallites formed on P25 and anatase are generally smaller than 20 nm (Fig. 3(c) and 4(c)), with the size of hcp Co^0 (<5 nm) being smaller than that of fcc Co^0. It can also be seen that the fcc Co^0 crystallites are larger than the starting Co_3O_4 crystallites, especially on the anatase support. There is a possibility that the metallic crystallites on P25 and anatase are composed of (partially) intergrown domains of fcc and hcp Co^0, which may help stabilise the small hcp Co^0 crystallites. Although the existence of intergrowth could not be confirmed using Rietveld refinement, this has been reported as a possible phenomenon by other researchers.[31,46,49]

We note that there is some degree of scatter in the Rietveld refinement data obtained for the co-existing fcc

 This journal is © The Royal Society of Chemistry 2023

Open Access Article. Published on 24 February 2023. Downloaded on 10/30/2025 4:25:35 AM.
This article is licensed under a Creative Commons Attribution 3.0 Unported Licence.

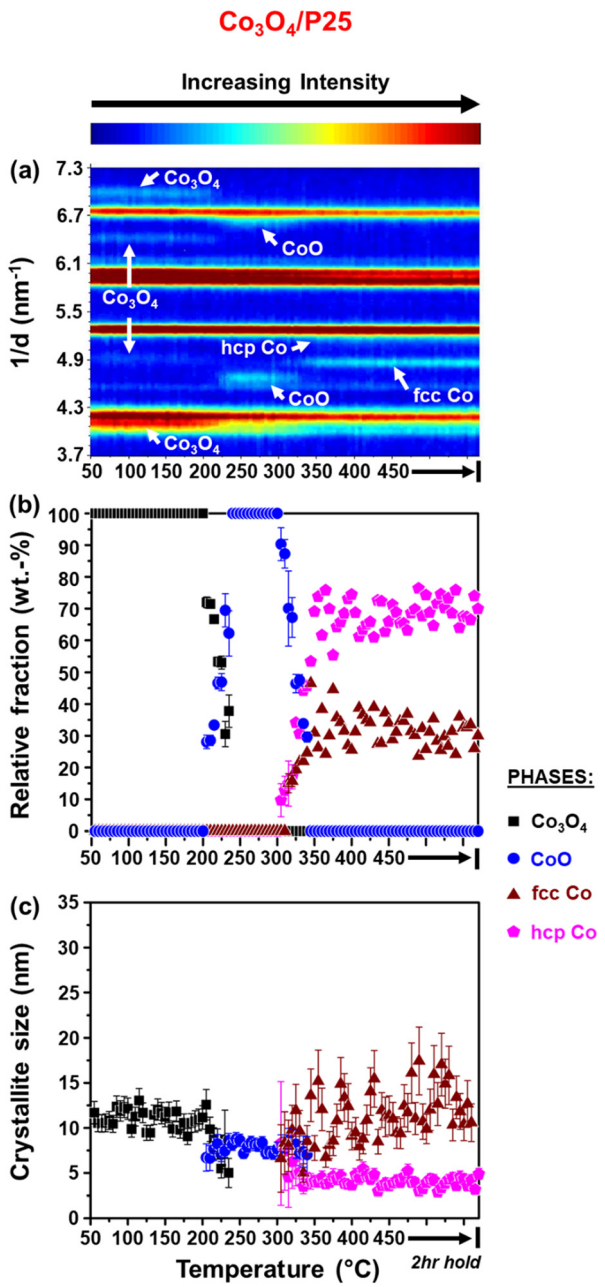

Fig. 3 (a) On-top view of the *in situ* PXRD patterns (X-ray source: Mo Kα1 = 0.07093 nm) recorded during the reduction of Co_3O_4/P25 (gas composition: 50% H_2 and 50% N_2; pressure: atmospheric; GHSV: 60 000 mL(NTP) $g_{Co_3O_4}^{-1}$ h^{-1}). (b) Relative weight fractions (with error bars) and (c) average crystallite sizes (with error bars) of the different Co-based phases detected (excluding the support).

and hcp Co^0 crystallites on P25 (Fig. 3(a) and (b)) and anatase (Fig. 4(a) and (b), right). This might be due to the inability to account for the possible (partial) intergrowth of the two Co^0 allotropes.[31] Furthermore, there is extensive overlap between the PXRD reflections of anatase, rutile (in P25), as well as fcc and hcp Co^0, which could also contribute to the scatter in the data. Nonetheless, for the P25- and anatase-supported catalysts, the relative fraction of hcp Co^0 is higher than that of fcc Co^0, with both catalysts exhibiting similar average hcp : fcc Co^0 ratios at 450 °C (*i.e.*, 2.3 for Co_3O_4/P25 and 1.8 for Co_3O_4/anatase).

3.2.2. Conventional H_2-TPR. H_2-TPR experiments were also performed to study the reduction behaviour of the prepared catalysts and bare supports between 60 and 920 °C, and the results obtained are presented in Fig. 5(a). The Co_3O_4 particles supported on P25 and rutile start reducing at a lower temperature (180 °C) than the particles supported on anatase (260 °C). This reduction trend is in line with the observations made during the PXRD-based reduction studies despite the differences in onset temperatures, which may be caused by the different experimental conditions applied (*e.g.*, different heating rates and concentrations of H_2 – see the section "*in situ* catalyst characterisation" in the ESI†).

The reduction profile of each catalyst displays multiple peaks between 200 and 660 °C, with some of the peaks appearing as broad and convoluted. Nonetheless, the P25- and rutile-supported catalysts may have undergone a stepwise reduction where Co_3O_4 first reduces to CoO, and then CoO reduces to Co^0.[5,8,45,50] The peak maxima at 270 °C for Co_3O_4/rutile and 280 °C for Co_3O_4/P25 may be assigned to the formation of CoO. The temperature ranges of 300–540 °C for Co_3O_4/rutile and 320–450 °C for Co_3O_4/P25 possibly represent the reduction to Co^0. However, the broad and convoluted nature of the reduction peaks in these temperature ranges may also suggest other contributing factors, such as particle size (or size distribution). In other words, different size CoO particles may be reducing at different temperatures, with larger particles reducing earlier.[28,43,44] It is also possible that some smaller Co_3O_4 particles reduce within the abovementioned temperature ranges, and not below 300 °C.

The reduction profile of Co_3O_4/anatase displays a small peak maximum at 300 °C possibly due to the reduction of a small amount of large Co_3O_4 particles. Between 330 and 490 °C, Co_3O_4/anatase also exhibits a broad reduction peak, which may be assigned to the reduction of relatively smaller Co_3O_4 particles to form metallic Co.[21,22] There may be some other CoO_x or $Co_xTi_yO_z$ species reducing between 500 and 660 °C (Fig. 5(a) and S9†) due to the existence of strong NPSI in this catalyst. The *in situ* formation of $Co_xTi_yO_z$ could have been facilitated by the partial surface reduction of anatase, followed by the migration and reaction of Ti_xO_y with CoO_x species.[7,10,16] Fig. 5(b) shows a partial reduction of the bare anatase support (possibly occurring in two steps) between 220 and 730 °C as well as 730 and 920 °C, unlike the bare P25 and rutile supports. However, the H_2 consumption of the bare anatase is almost negligible when compared with that of the supported Co_3O_4 catalysts (Fig. 5(a)). The degree of reduction (DoR) to Co^0 of each supported Co_3O_4 catalyst was calculated using eqn (S12)–(S14)† and the results are presented in Table 2. The DoR trend is as follows: Co_3O_4/P25 (92.5%) > Co_3O_4/rutile (90.3%) > Co_3O_4/anatase (85.5%), which suggests a higher proportion of unreduced Co-based oxides on the anatase support, likely due to the existence of strong NPSI.

Open Access Article. Published on 24 February 2023. Downloaded on 10/30/2025 4:25:35 AM.
This article is licensed under a Creative Commons Attribution 3.0 Unported Licence.

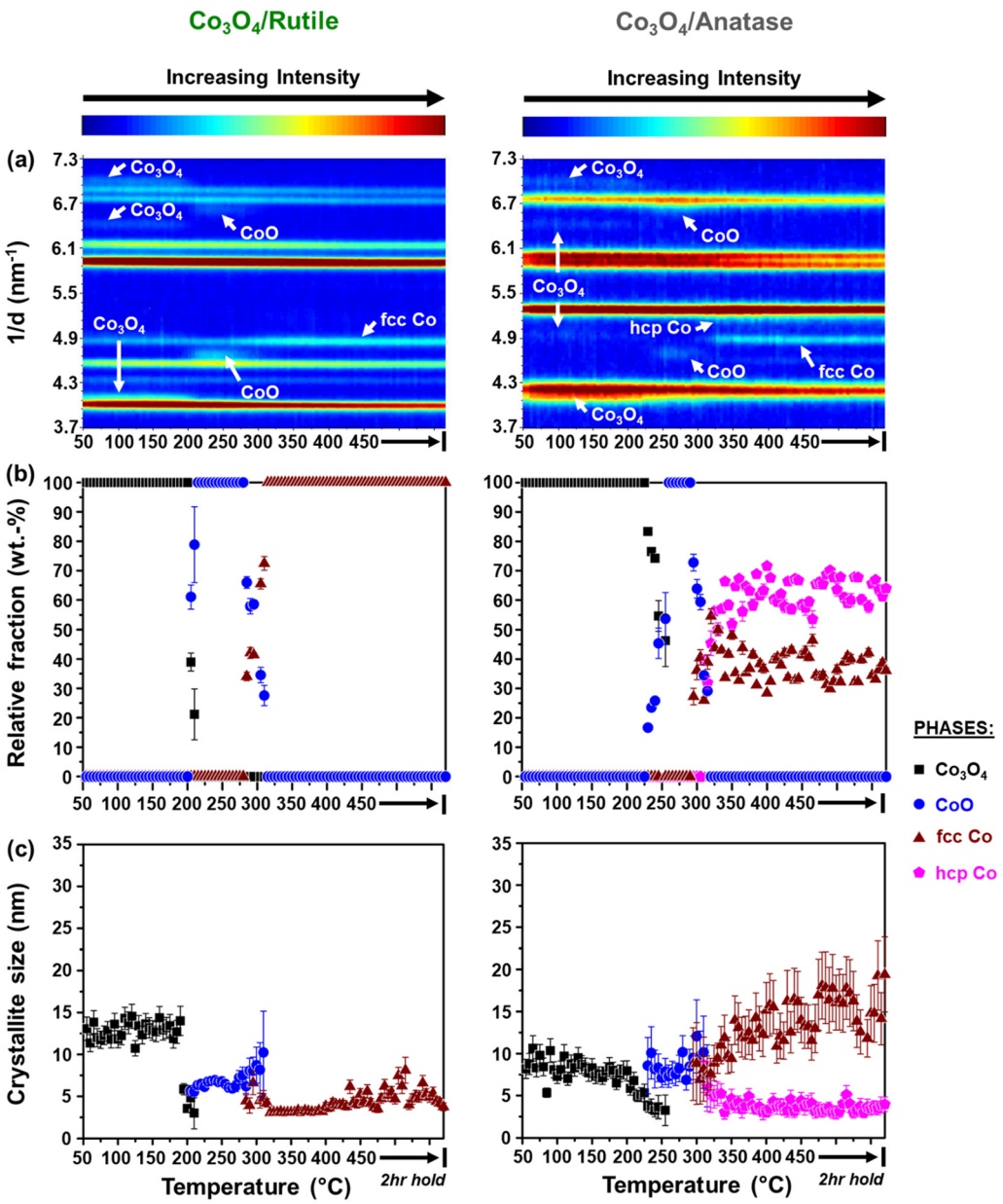

Fig. 4 (a) On-top view of the *in situ* PXRD patterns (X-ray source: Mo Kα1 = 0.07093 nm) recorded during the reduction of (left) Co_3O_4/rutile and (right) Co_3O_4/anatase (gas composition: 50% H_2 and 50% N_2; pressure: atmospheric; GHSV: 60 000 mL(NTP) $g_{Co_3O_4}^{-1}$ h^{-1}). (b) Relative weight fractions (with error bars) and (c) average crystallite sizes (with error bars) of the different Co-based phases detected (excluding the supports).

3.3. *In situ* catalyst characterisation and evaluation

The activity and selectivity of the TiO_2-supported catalysts were evaluated under model/dry CO-PrOx conditions, which involved co-feeding 1% CO, 1% O_2, 50% H_2, and 48% N_2 at a GHSV of 60 000 mL(NTP) $g_{Co_3O_4}^{-1}$ h^{-1}. The temperature was varied stepwise between 50 and 450 °C at atmospheric pressure while analysing the reactor effluent gas using on-line gas chromatography. Furthermore, the catalysts were characterised *in situ* using PXRD and magnetometry to monitor their chemical and crystallographic phase changes. Fig. 6(a) and 7(a) show the calculated relative weight fractions of the Co-based crystalline phases detected using PXRD, and Fig. 6(b) and 7(b) show the crystallite sizes of the detected phases as a function of temperature for all three catalysts. The recorded diffraction patterns are plotted in Fig. S10.† Fig. 6(c) and 7(c) display the normalised gas outlet flow rates of CO, O_2, CO_2, and CH_4; while Fig. 8(a)–(c) display a summary of the CO conversion to CO_2 ($X_{CO\rightarrow CO_2}$), O_2 selectivity to CO_2 ($S_{O_2\rightarrow CO_2}$), and CO conversion to CH_4 ($X_{CO\rightarrow CH_4}$), respectively. The magnetometry-derived DoR of Co_3O_4 to Co^0 is plotted in Fig. 6(d), 7(d), and 8(d) for all evaluated catalysts. The DoR was calculated using eqn (S15),† which is based on an instrument calibration curve (Fig. S2†). The $X_{CO\rightarrow CO_2}$ and $X_{CO\rightarrow CH_4}$ values for the bare TiO_2 supports can be found in Fig. S11.†

Open Access Article. Published on 24 February 2023. Downloaded on 10/30/2025 4:25:35 AM.
This article is licensed under a Creative Commons Attribution 3.0 Unported Licence.

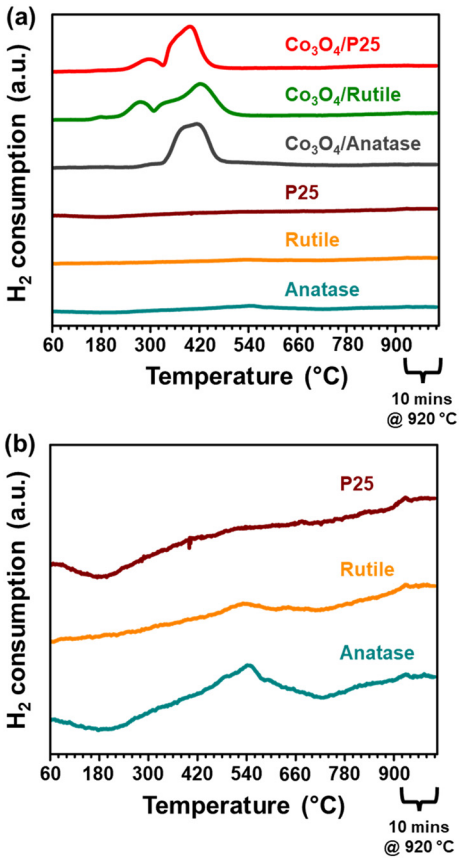

Fig. 5 Reduction profiles of the (a) Co_3O_4-loaded and bare TiO_2 support materials derived from H_2-TPR performed in a 5 : 95 H_2 : Ar mixture at atmospheric pressure. (b) A re-plot of the reduction profiles of the bare support materials.

Table 2 Degree of reduction of each supported catalyst after H_2-TPR

Sample name	DoR (%)
Co_3O_4/P25	92.5
Co_3O_4/rutile	90.3
Co_3O_4/anatase	85.3

Below 200 °C, the normalised outlet flow rates of CO and O_2 decrease while the outlet flow of CO_2 increases with increasing temperature, which confirms the oxidation of CO to CO_2 over all three catalysts. However, at 200 °C, the outlet flow of CO reaches a minimum (correspondingly, the $X_{CO\rightarrow CO_2}$ reaches a maximum (Fig. 8(a))), while the outlet flow of O_2 continues to decrease until reaching zero at 225 °C for Co_3O_4/P25 (Fig. 6(c)) and 250 °C for Co_3O_4/rutile and Co_3O_4/anatase (Fig. 7(c)). According to eqn (1), half a mole of O_2 is required to convert one mole of CO to one mole of CO_2. In the current experiments, a 1 : 1 CO : O_2 feed ratio was used, implying that the conversion of O_2 should ideally be half of the conversion of CO. However, the continued decrease in the outlet flow of O_2 suggests the simultaneous occurrence of H_2 oxidation (eqn (2)), which is a well-known competing reaction in CO-PrOx.[23,24,27–33] This is also confirmed by the $S_{O_2\rightarrow CO_2}$, which is below 100% from 75 °C for all three catalysts and continues to decrease as the reaction temperature is increased (Fig. 8(b)).

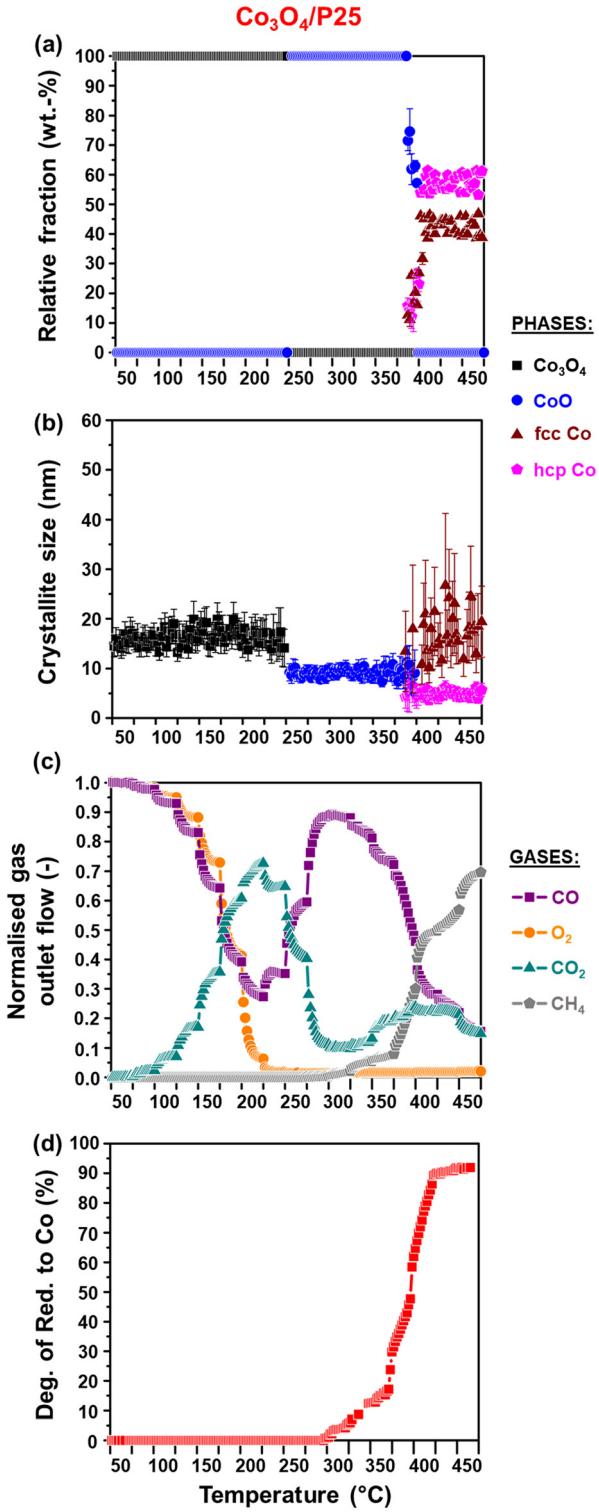

Fig. 6 (a) Relative weight fractions and (b) average crystallite sizes of the different Co-based phases detected using PXRD (excluding the support). (c) Normalised outlet flow rates of CO, O_2, CO_2, and CH_4. (d) Magnetometry-derived DoR of Co_3O_4 to Co^0 obtained for Co_3O_4/P25 during CO-PrOx (gas composition: 1% CO, 1% O_2, 50% H_2, and 48% N_2; pressure: atmospheric; GHSV: 60 000 mL(NTP) $g_{Co_3O_4}^{-1}$ h^{-1}).

Open Access Article. Published on 24 February 2023. Downloaded on 10/30/2025 4:25:35 AM.
This article is licensed under a Creative Commons Attribution 3.0 Unported Licence.

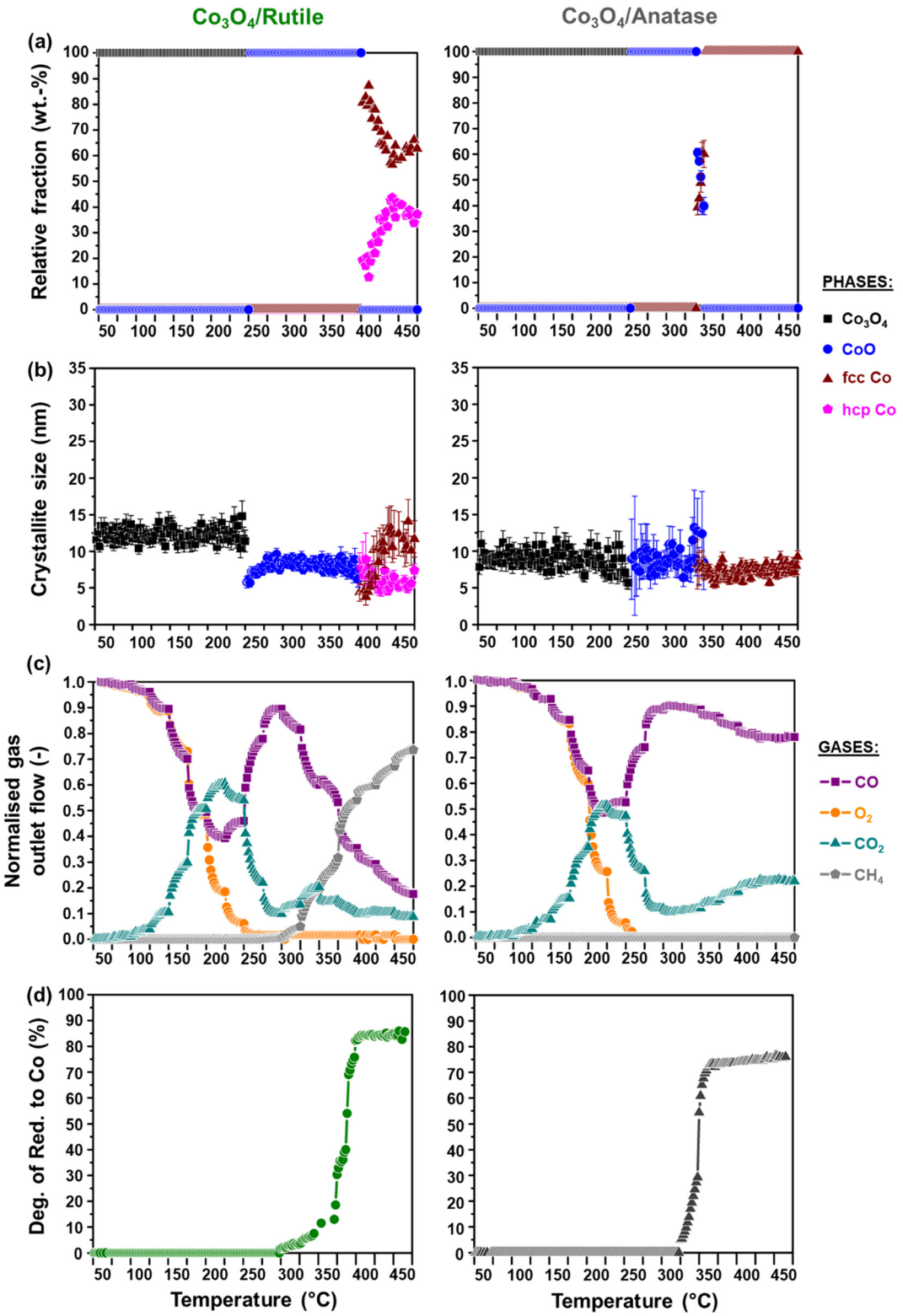

Fig. 7 (a) Relative weight fractions and (b) average crystallite sizes of the different Co-based phases detected using PXRD (excluding the supports). (c) Normalised outlet flow rates of CO, O_2, CO_2, and CH_4. (d) Magnetometry-derived DoR of Co_3O_4 to Co^0 obtained for (left) Co_3O_4/rutile and (right) Co_3O_4/anatase during CO-PrOx (gas composition: 1% CO, 1% O_2, 50% H_2, and 48% N_2; pressure: atmospheric; GHSV: 60 000 mL(NTP) $g_{Co_3O_4}^{-1}$ h^{-1}).

$$CO(g) + 1/2O_2(g) \rightarrow CO_2(g) \quad \Delta H^{\circ}_{298.15K} = -283.0 \text{ kJ mol}^{-1} \quad (1)$$

$$H_2(g) + 1/2O_2(g) \rightarrow H_2O(g) \quad \Delta H^{\circ}_{298.15K} = -241.9 \text{ kJ mol}^{-1} \quad (2)$$

Open Access Article. Published on 24 February 2023. Downloaded on 10/30/2025 4:25:35 AM.
This article is licensed under a Creative Commons Attribution 3.0 Unported Licence.

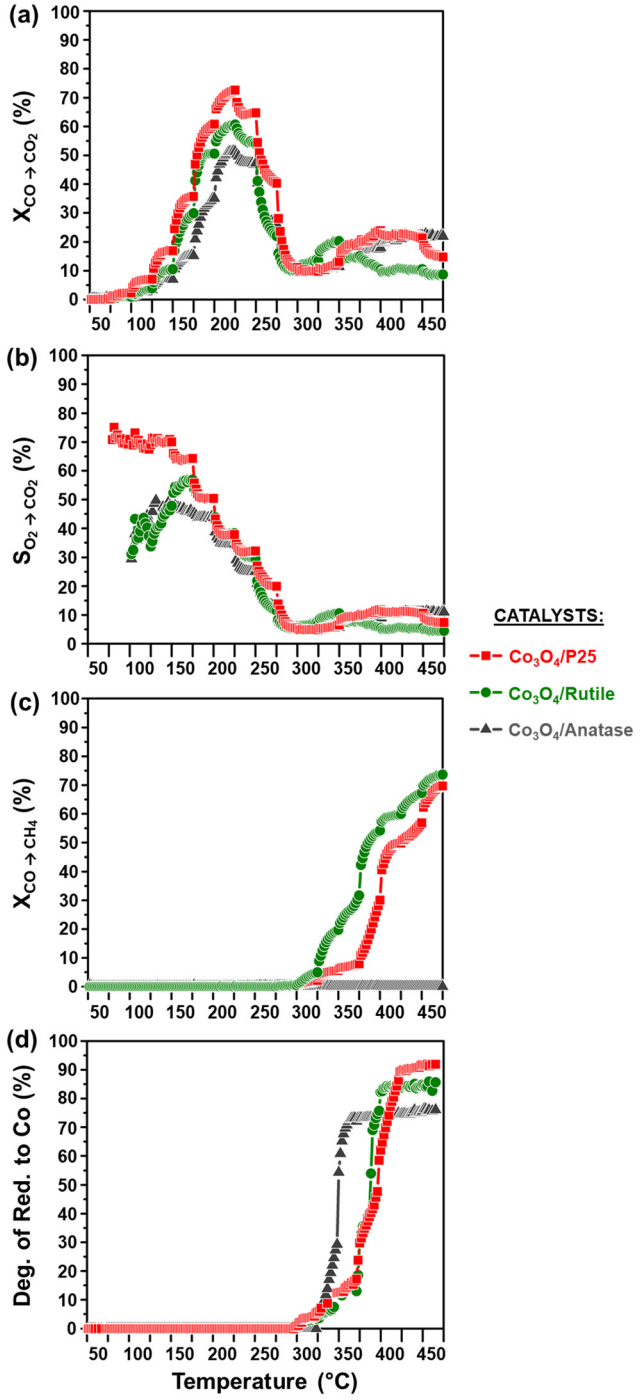

Fig. 8 (a) CO conversion to CO_2 ($X_{CO\rightarrow CO_2}$), (b) O_2 selectivity to CO_2 ($S_{O_2\rightarrow CO_2}$), (c) CO conversion to CH_4 ($X_{CO\rightarrow CH_4}$), and (d) magnetometry-derived DoR of Co_3O_4 to Co^0 during CO-PrOx for all prepared catalysts. The $S_{O_2\rightarrow CO_2}$ was calculated at temperatures where both CO and O_2 were converted (see Fig. 6(c), 7(c), and 8(a)). (Gas composition: 1% CO, 1% O_2, 50% H_2, and 48% N_2; pressure: atmospheric; GHSV: 60 000 mL(NTP) $g_{Co_3O_4}^{-1}h^{-1}$).

A comparison of the CO oxidation activities of the evaluated catalysts shows that Co_3O_4/P25 is the most active catalyst over a wide temperature range (50 and 275 °C) and reaches a maximum $X_{CO\rightarrow CO_2}$ of 72.7% at 200 °C, followed by Co_3O_4/rutile (60.7%) and Co_3O_4/anatase (51.5%) at the same temperature. The Co_3O_4/P25 catalyst also exhibits better $S_{O_2\rightarrow CO_2}$ values between 50 and 275 °C than the rutile- and anatase-supported catalysts. Although the catalysts do not reach the desired minimum $X_{CO\rightarrow CO_2}$ of 99.9% (*i.e.*, decreasing the concentration of CO below 10 ppm),[23,24] P25 may still be a viable support for future catalyst development work in the context of CO-PrOx. This support composes of a mixture of rutile (15%) and anatase (85%), which has improved the activity of catalysts used in other catalytic processes.[21] The mixture of rutile and anatase is thought to result in relatively weaker interactions with Co_3O_4 nanoparticles, making them easier to reduce.[21,22] Therefore, assuming the MvK mechanism for CO oxidation, which involves a surface reduction–oxidation (redox) cycle being undergone by Co_3O_4,[25,26] the higher activity of Co_3O_4/P25 may be due to the existence of weak NPSI that allow for an effective surface redox cycle.

Fig. S11(a)† shows the $X_{CO\rightarrow CO_2}$ values plotted as a function of temperature for the three bare supports. It can be seen that the bare supports also exhibit some CO oxidation activity, with $X_{CO\rightarrow CO_2}$ values that are below 10%. However, the Co_3O_4-loaded supports display much higher $X_{CO\rightarrow CO_2}$ values than those of the bare supports, which emphasises the importance of the Co_3O_4 phase. There may be contributions to the CO oxidation activity from each support, but this can be expected to be minor.

Based on the *in situ* PXRD measurements performed (Fig. 6, 7, and S10†), the Co_3O_4 phase is stable between 50 and 225 °C in all three catalysts, which explains the overall increase in the $X_{CO\rightarrow CO_2}$ values within this temperature range. However, it is possible that the slight decrease in the $X_{CO\rightarrow CO_2}$ observed for all three catalysts from 225 °C (Fig. 6(c), 7(c), and 8(a)) is caused by the reduction of the Co_3O_4 surface to CoO,[27–32] despite this being undetected using bulk-sensitive PXRD. Furthermore, the increase in the amount of O_2 converted *via* H_2 oxidation might also explain the decrease in the $X_{CO\rightarrow CO_2}$ values from 225 °C. With reference to the MvK mechanism, the ultimate depletion of O_2 at 225 °C for Co_3O_4/P25 and 250 °C for Co_3O_4/rutile and Co_3O_4/anatase may have led to the onset formation of CoO at these temperatures as there was no O_2 available to stabilise (or regenerate) the active Co_3O_4 phase.[25,26]

In situ PXRD adequately shows the formation of CoO at 250 °C in all three catalysts, which is later converted to fcc Co^0 on anatase (325 °C) and to fcc and hcp Co^0 on P25 (375 °C) and rutile (400 °C) (Fig. 6, 7, S10, and S12†). However, Co^0 (with no distinction between fcc and hcp Co^0) is detected earlier in the magnetometer, that is, at 300 °C for the P25- and rutile-supported catalysts, and at 325 °C for the anatase-supported catalyst (see DoR plots in Fig. 6(d), 7(d), and 8(d)). As stated in section 2.2.2., the magnetometer is more sensitive than PXRD, which explains the earlier detection of Co^0 on P25 and rutile during the magnetometry-based experiments.[28–32] It can also be observed that within the temperature range where CoO exists in each catalyst, the amount of CO converted to CO_2 decreases with increasing temperature, indicating that CoO catalyses H_2 oxidation to a greater extent.[27–32]

Open Access Article. Published on 24 February 2023. Downloaded on 10/30/2025 4:25:35 AM.
This article is licensed under a Creative Commons Attribution 3.0 Unported Licence.

Upon forming Co^0, CO is converted to CH_4, which is an undesired CO conversion pathway because valuable H_2 is being consumed (eqn (3)).[27–33] However, methanation only takes place over the fcc and hcp Co^0 formed on P25 (max. $X_{CO\rightarrow CH_4}$: 69.7% at 450 °C) and rutile (max. $X_{CO\rightarrow CH_4}$: 73.7% at 450 °C), and not over the fcc Co^0 formed on anatase (Fig. 8(c)). The bare P25 and rutile supports also exhibit $X_{CO\rightarrow CH_4}$ values that are below 1%, with the anatase support displaying no methanation activity (Fig. 11(b)). At this stage, we propose that the metallic particles on anatase may be encapsulated by Ti_xO_y species, thereby blocking active sites on fcc Co^0, which has been observed for a reduced Co/anatase catalyst used in the FTS.[16] The encapsulation is thought to be driven by the more facile reduction of anatase (also see H_2-TPR profile in Fig. 5(b)), followed by the migration of Ti_xO_y species to the surface of fcc Co^0 due to the significant differences in their surface energies (anatase: 0.44 J m^{-2}, and fcc Co^0: 2.6 J m^{-2}).[13–15] Evidence for Co encapsulation in this study, based on STEM-EELS analysis, is discussed in section 3.4.2.

$$CO(g) + 3H_2(g) \rightarrow CH_4(g) + H_2O(g) \quad \Delta H^{\circ}_{298.15K} = -206.2\ \text{kJ mol}^{-1} \tag{3}$$

Although considerable amounts of CH_4 are formed between 300 and 450 °C over the Co^0 allotropes on P25 and rutile, there is also some CO_2 being formed, with $X_{CO\rightarrow CO_2}$ values that are less than 25% being achieved (Fig. 8(a)). Co^0 is not known for catalysing CO oxidation but there is a possibility of an *in situ* water-gas shift (WGS) reaction taking place on the metallic surface, which first involves the formation of H_2O *via* H_2 oxidation, followed by the reaction of this H_2O with CO (eqn (4)).[29,31,32] Additionally, the direct oxidation of CO could be taking place over the unreduced CoO in the P25- and rutile-supported catalysts[51–53] since they are not fully reduced even at 450 °C based on the magnetometry results (max. DoRs: 91.9% for Co_3O_4/P25 and 85.9% for Co_3O_4/rutile). The same could apply to the unreduced CoO present on anatase (max. DoR: 76.4% at 450 °C). At this stage, it is unclear if the encapsulated fcc Co^0 particles on anatase catalyse the formation of CO_2 *via* CO oxidation, the WGS, or any other reaction pathway.

$$CO(g) + H_2O(g) \rightleftharpoons CO_2(g) + H_2(g) \quad \Delta H^{\circ}_{298.15K,forward} = -41.1\ \text{kJ mol}^{-1} \tag{4}$$

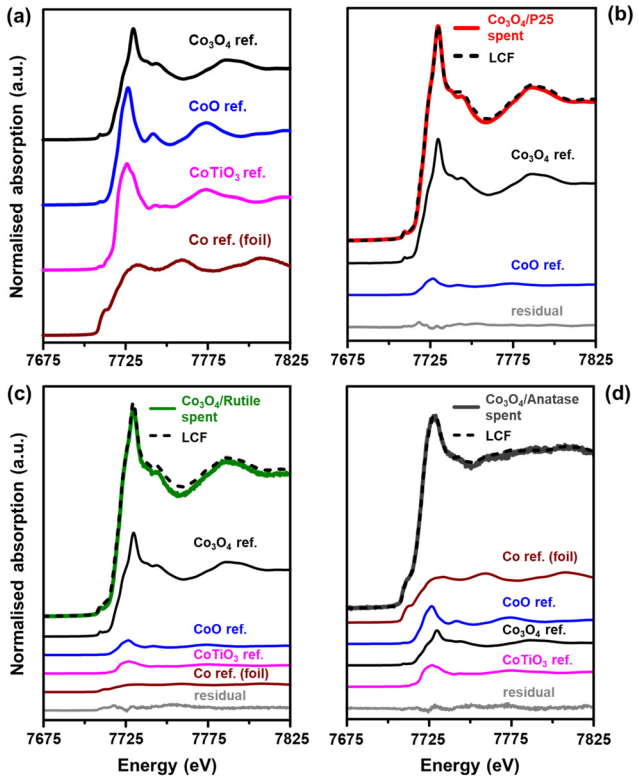

Fig. 9 Normalised XANES spectra of the (a) reference compounds and (b)–(d) spent samples obtained after performing CO-PrOx. The results from the LCF are also included in (b)–(d). The fitted reference components in (b)–(d) are scaled according to their contribution to the LCF.

Unlike magnetometry, the PXRD measurements indicate a complete reduction of CoO to Co^0 in all three catalysts at 450 °C (Fig. 6, 7, and S10†). As mentioned earlier, PXRD requires higher amounts of crystalline material for adequate detection, so it is possible that the remaining unreduced CoO is below the detection limit of PXRD (typically 2–3 wt%). Nonetheless, PXRD provides important crystallographic information (*e.g.*, a distinction between fcc and hcp Co^0 can be made), making it a suitable complementary technique to magnetometry. It is worth mentioning that during the PXRD-based reduction studies, Co_3O_4 ultimately reduced to fcc and hcp Co^0 only on P25 and anatase (Fig. 3 and 4), while during CO-PrOx, Co_3O_4 reduces to both allotropes only on P25 and rutile.

Sławiński *et al.*[46] and Nyathi *et al.*[31] have shown that the formation of fcc and hcp Co^0 (with different ratios) can be influenced by the gas environment. Although this effect was not investigated in-depth, the idea is that different reducing environments may cause the reduction to occur at different temperatures and reduction rates. Consequently, the metallic particles formed can also differ in size, leading to the formation of particles with crystalline domains of either one or both allotropes of Co. Additionally, the strength of the NPSI may influence the reduction of cobalt oxide particles (*i.e.*, Co_3O_4 and CoO) depending on their size and the type of support used.[10,30,32,45] Therefore, the formation of fcc and hcp Co^0 on anatase (during the PXRD-based reduction studies only) and rutile (during CO-PrOx only) might have been caused by the different gas environments and the nature of the interactions between these supports and the Co_3O_4/CoO particles. Moreover, these effects may have also resulted in the higher hcp Co^0 content relative to fcc Co^0 on P25 (hcp : fcc ratio: 1.3 at 450 °C), while more fcc Co than hcp Co^0 is formed on rutile (hcp : fcc ratio: 0.5 at 450 °C) during CO-PrOx (Fig. 6(a) and 7(a)). Similar to the PXRD-based reduction experiments, Rietveld refinement could not be used to confirm fcc–hcp Co^0 intergrowth, but the occurrence of this phenomenon cannot be ruled out.[31,46,49]

Open Access Article. Published on 24 February 2023. Downloaded on 10/30/2025 4:25:35 AM.
This article is licensed under a Creative Commons Attribution 3.0 Unported Licence.

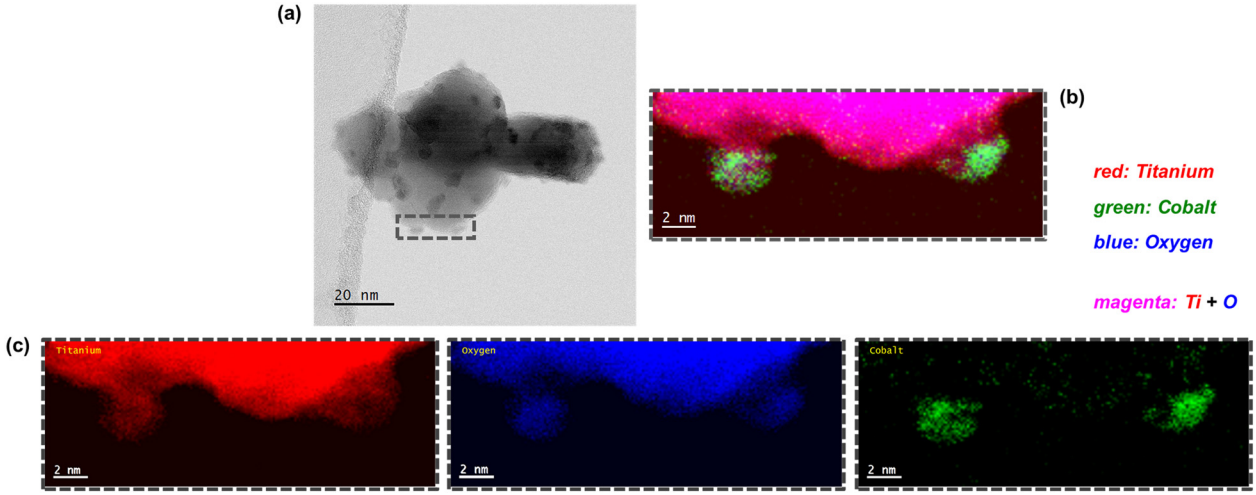

Fig. 10 (a) Bright-field STEM micrograph, (b) magnified STEM-EELS composite map showing the regions with Ti, O, and Co, and the (c) corresponding magnified STEM-EELS maps of the individual elements present in the spent Co_3O_4/anatase catalyst.

The reduction of Co_3O_4 on all support materials leads to the formation of CoO crystallites of similar sizes (on anatase) or smaller sizes (on P25 and rutile) than the starting Co_3O_4 crystallites (Fig. 6(b) and 7(b)), indicating minimal or no sintering. On anatase, the fcc Co^0 crystallites are also similar in size as the CoO and Co_3O_4 crystallites, further confirming no significant crystallite growth. However, the fcc Co^0 crystallites formed on P25 and rutile are larger than the crystallites of CoO, while hcp Co^0 is smaller than CoO. As observed during the magnetometry studies, the P25- and rutile-supported catalysts achieved higher DoRs than the anatase-supported catalyst (Fig. 6(d), 7(d), and 8(d)), which may suggest the existence of weaker NPSIs in the highly reduced catalysts.[10,30,32,45] It is also possible that the sintering of fcc Co^0 on P25 and rutile is a result of the weak NPSIs.[54]

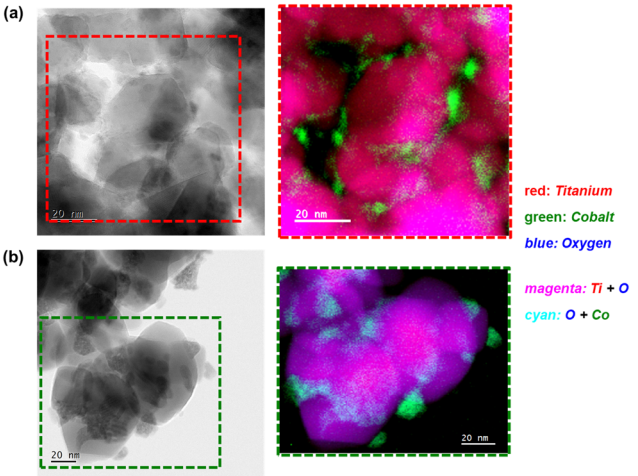

Fig. 11 (Left) Bright-field STEM micrographs and the (right) magnified STEM-EELS composite maps showing the regions with Ti, O, and Co in the spent (a) Co_3O_4/P25 and (b) Co_3O_4/rutile catalysts.

3.4. *Ex situ* characterisation of spent catalysts

3.4.1. XAS measurements. *Ex situ* XAS measurements were conducted primarily to determine the presence of mixed metal oxides (such as $CoTiO_3$) in the spent catalysts. Since $CoTiO_3$ is not ferromagnetic,[55] it would not be detected using magnetometry. Although $CoTiO_3$ is detectable using PXRD, the *in situ* diffraction patterns obtained for all catalysts during CO-PrOx did not show any reflections from this phase (Fig. S10†), possibly due to its formation in small amounts and/or small crystallite sizes.

The normalised XANES (X-ray absorption near edge structure) spectra of the reference compounds Co_3O_4,[44] CoO,[56] $CoTiO_3$,[57] and Co^0 (or Co foil)[58] are presented in Fig. 9(a). These reference compounds were synthesised according to the procedures outlined in the cited literature. The first derivatives of the XANES spectra for the reference compounds (Fig. S13†) also help to show the differences in their spectral features. Fig. 9(b)–(d) shows the XANES spectra of the spent catalysts together with the linear combination fit (LCF) and the individual fitted components, which have been scaled according to their contribution to the LCF. The phase compositions of the spent samples (based on the LCF) are presented in Table 3 together with the *R*-factors. It is worth mentioning that the quantities of the Co-based phases reported in Table 3 are on a Co basis because only the Co K-edge was measured. Therefore, the amounts of the different Co-based phases can be expected to be much lower than those presented in Table 3 after factoring in the proportion of the support, which is at least 90 wt% according to ICP-OES analysis.

The results of the LCF generally indicate a high concentration of Co_3O_4 in each spent sample, whereas the *in situ* PXRD experiments showed the complete disappearance of this phase to CoO and Co^0 during CO-PrOx (Fig. 6, 7, and S10†). Therefore, the presence of Co_3O_4 in the spent samples analysed using XAS is likely due to the re-oxidation of the CoO

Open Access Article. Published on 24 February 2023. Downloaded on 10/30/2025 4:25:35 AM.
This article is licensed under a Creative Commons Attribution 3.0 Unported Licence.

Table 3 Results obtained after performing linear combination fitting on the normalised XANES spectra

Sample name	Co_3O_4 (%)	CoO (%)	$CoTiO_3$ (%)	Co^0 (%)	*R*-Factor (–)
Co_3O_4/P25 spent	88.9 ± 0.9	11.1 ± 0.6	—	—	0.003
Co_3O_4/rutile spent	73.0 ± 6.1	9.8 ± 3.6	8.9 ± 4.5	8.3 ± 1.2	0.010
Co_3O_4/anatase spent	21.3 ± 0.7	21.8 ± 1.5	13.8 ± 1.8	43.2 ± 2.5	0.002

and Co^0 during the long storage times (6–12 months) of the samples in a non-inert environment prior to the XAS measurements. However, since determining the presence of mixed metal oxides using XAS was of primary importance, these oxides would remain stable during sample storage and therefore, should still be detectable.[10,57]

The Co_3O_4/P25 spent catalyst underwent extensive re-oxidation as the XANES spectrum mostly exhibits features similar to those of Co_3O_4 between 7700 and 7825 eV (Fig. 9(b)). The LCF also confirmed the presence of 88.9 ± 0.9% Co_3O_4 and 11.1 ± 0.6% CoO, with no traces of $CoTiO_3$. The spectrum of the rutile-supported spent catalyst (Fig. 9(c)) is also dominated by features of the Co_3O_4 phase (73.0 ± 6.1%), but also shows an edge shift of approximately 1.5 eV to the left, relative to the main edge of the Co_3O_4 reference (which is at 7723 eV). This left shift is indicative of Co species of lower oxidation state, that is, below +3. Indeed, there are also relatively small amounts of CoO (9.8 ± 3.6%), $CoTiO_3$ (8.9 ± 4.5%), and Co^0 (8.3 ± 1.2%) in the Co_3O_4/rutile spent catalyst. In these three phases, Co is either in the +2 or 0 oxidation state.

The XANES spectrum of Co_3O_4/anatase (Fig. 9(d)) exhibits different features from those observed in the spectra of Co_3O_4/P25 and Co_3O_4/rutile. There is a pronounced pre-edge feature at 7710 eV, which indicates the presence of Co^0, and the edge and white line have shifted to the left by approximately 3 eV relative to the edge and white line of the Co_3O_4 reference (which are at 7723 and 7730 eV, respectively). The white line and the spectral features between 7750 and 7825 eV for Co_3O_4/anatase appear to be less intense (Fig. 9(d)). These observations further indicate the presence of relatively high amounts of Co^0 (43.2 ± 2.5%) in this spent sample. There is also CoO (21.8 ± 1.5%), Co_3O_4 (21.3 ± 0.7%), and $CoTiO_3$ (13.8 ± 1.8%) indicated by the LCF.

The presence of $CoTiO_3$ in the Co_3O_4/rutile and Co_3O_4/anatase spent catalysts is in good agreement with the low magnetometry-derived DoRs reached by these samples (85.9% and 76.4%, respectively) at 450 °C during CO-PrOx when compared with Co_3O_4/P25 (91.9%), which did not form $CoTiO_3$. We note that $CoTiO_3$ was not observed in any supported catalyst during the PXRD-based *in situ* reduction or CO-PrOx experiments. This may have been a result of the $CoTiO_3$ amounts being below the detection limit of the PXRD instrument. Nonetheless, the higher content of $CoTiO_3$ in Co_3O_4/anatase is possibly due to the high reduction susceptibility of anatase (also see H_2-TPR profile in Fig. 6(b)) followed by the migration and reaction of Ti_xO_y with CoO_x species.[7,10,16] Rutile is generally less susceptible to reduction, which might explain the lower amounts of $CoTiO_3$ formed in Co_3O_4/rutile. The more facile formation of $CoTiO_3$ in Co_3O_4/anatase is also supported by thermodynamic calculations (based on bulk phases), which show lower values for the change in the Gibbs free energy (ΔG) and partial pressure ratio of H_2-to-H_2O (p_{H_2}/p_{H_2O}) as a function of temperature than for Co_3O_4/rutile (Fig. S14 and S15†). The P25 support is a 15 : 85 mixture of rutile and anatase, which is thought to make the support (or the anatase fraction) more stable under reduction conditions.[21,22] This could explain the absence of $CoTiO_3$ in the Co_3O_4/P25 spent sample.

3.4.2. STEM-EELS analysis. The spent catalysts were also studied using STEM-EELS to determine changes in particle size in comparison with the fresh catalysts. Fig. 10 and 11 show the bright-field micrographs of the three spent samples as well as the corresponding elemental maps showing regions with Ti, O, and Co. PXRD measurements carried out during CO-PrOx indicated the presence of fcc and hcp Co^0 crystallites at 450 °C that vary between 10 and 25 nm for the fcc phase, and between 5 and 10 nm for the hcp phase, among the three evaluated catalysts (Fig. 6(b) and 7(b)). Although the spent samples that were analysed using STEM-EELS likely underwent re-oxidation during storage, the particles shown in Fig. 10 and 11 are mostly below 10 nm, which is smaller than the starting Co_3O_4 particles (Table 1).

The exact cause of the size discrepancy between PXRD and STEM-EELS (especially regarding fcc Co^0) remains unknown. However, it is possible that there exists a small number of large particles that were not identified using STEM-EELS, but were detected using PXRD, resulting in larger average sizes for fcc Co^0 based on PXRD. Furthermore, in the absence of fcc–hcp Co^0 intergrowth, the small particles identified using STEM-EELS could be hcp Co^0 (although this is thermodynamically less feasible[47,48]), or could have been derived from hcp Co^0, in the case of re-oxidation during sample storage.[31]

Interestingly, some of the small Co-bearing particles located on the edge of the large anatase particles have been encapsulated by Ti_xO_y species (Fig. 10 and S16†). This is not observed in the STEM-EELS micrographs of the Co_3O_4/P25 and Co_3O_4/rutile spent samples (Fig. 11). The encapsulation of CoO_x particles by anatase-derived Ti_xO_y species is well-known under reducing conditions,[7,10,16] but this is being observed after CO-PrOx for the first time in this study. In section 3.3., it was proposed that the absence of CH_4 in the CO-PrOx product stream of Co_3O_4/anatase (Fig. 7(c)) was due to the encapsulation of Co^0 (or more generally, CoO_x species). Therefore, the detection of Ti_xO_y-encapsulated Co-bearing particles using STEM-EELS could explain the absence of CH_4 formation over the partially reduced anatase-supported catalyst. Furthermore, it has been reported that the encapsulation of CoO_x particles by Ti_xO_y species may lead to

 This journal is © The Royal Society of Chemistry 2023

Open Access Article. Published on 24 February 2023. Downloaded on 10/30/2025 4:25:35 AM.
This article is licensed under a Creative Commons Attribution 3.0 Unported Licence.

the formation of $CoTiO_3$.[7,10,16] This phase was detected in relatively high amounts (13.8 ± 1.8%) in the Co_3O_4/anatase spent sample using XAS.

4. Conclusions

The presented study investigated the effect of different TiO_2 polymorphs (rutile, anatase, and a 15 : 85 mixture of rutile and anatase (also commercially known as P25)), used as supports, on the chemical and crystallographic phase transformations of Co_3O_4 during dry CO-PrOx. The phase changes were detected *in situ* using PXRD and magnetometry as a function of temperature, while *ex situ* XAS and STEM-EELS analyses of the spent catalysts provided further complementary information on the phase changes that occurred. Furthermore, on-line gas product analysis was coupled with the *in situ* characterisation to evaluate catalytic performance. It was shown that supporting Co_3O_4 on P25 results in high CO conversions to CO_2, with a maximum conversion of 72.7% achieved at 200 °C. Owing to the high concentrations of H_2 in the feed (50%), the reduction of Co_3O_4 to CoO and ultimately to Co^0 took place in all three catalysts, which caused a loss in the CO_2 yield and selectivity. The DoR of Co_3O_4 to Co^0 was highest on P25 (91.9% at 450 °C), while the DoR (76.4% at 450 °C) and CO_2 yield (51.5% at 200 °C) was lowest on anatase. Assuming the MvK mechanism for CO oxidation, which depends on surface reduction (and re-oxidation), the high CO oxidation activity of Co_3O_4/P25 could be a result of its high surface reducibility. Furthermore, the high surface and bulk reducibility (as determined *via in situ* characterisation for the latter) of Co_3O_4/P25 could be due to the existence of weak interactions between the Co_3O_4 nanoparticles and P25 support.

The Co^0 formed on P25 and rutile existed in the fcc and hcp crystal forms at elevated temperatures during CO-PrOx, while only fcc Co^0 was formed on anatase. The average larger size of Co^0 crystallites, relative to the size of CoO crystallites, on P25 and rutile may have led to the formation of (partially) intergrown crystalline domains of fcc and hcp Co^0. This sintering may have also been a result of the weaker NPSIs in Co_3O_4/P25 and Co_3O_4/rutile when compared with the NPSIs in Co_3O_4/anatase. The formation of $CoTiO_3$ was confirmed in the anatase (13.8%) and rutile (8.9%) supported spent catalysts *via ex situ* XAS, while the presence of Ti_xO_y-encapsulated CoO_x particles was only observed in the anatase-supported spent catalyst *via ex situ* STEM-EELS. The encapsulation of CoO_x particles may have occurred because of the relatively high reducibility of the anatase support, which forms highly mobile Ti_xO_y species that migrate to the surface of the CoO_x particles. In the case of the encapsulated fcc Co^0 particles on anatase, CH_4 formation did not take place (even at 450 °C) as the required surface active sites may have been blocked. On the other hand, CH_4 formation was observed over the fcc and hcp Co^0 on P25 and rutile, possibly because of minimal or no encapsulation.

Conflicts of interest

There are no conflicts to declare.

Acknowledgements

Johnson Matthey, the DSI-NRF Centre of Excellence in Catalysis (c*change), and the Science and Technology Facilities Council (STFC) *via* GCRF-START (Global Challenges Research Fund – Synchrotron Techniques for African Research and Technology (ST/R002754/1)) are gratefully acknowledged for their financial support. The authors would also like to thank the staff in the Analytical Laboratory, within the Chemical Engineering department (University of Cape Town), for conducting the ICP-OES analysis. Finally, M. Panchal (University College London and UK Catalysis Hub) and Dr. N. Ramanan (Diamond Light Source) are thanked for assisting with the XAS measurements on beamline B18 at Diamond Light Source (sessions: SP19850-3, SP19850-4, and SP19850-5).

References

1 S. Farrokhpay, *Adv. Colloid Interface Sci.*, 2009, **151**, 24–32.
2 A. Jaroenworaluck, W. Sunsaneeyametha, N. Kosachan and R. Stevens, *Surf. Interface Anal.*, 2006, **38**, 473–477.
3 A. Fujishima and K. Honda, *Nature*, 1972, **238**, 37–38.
4 D. A. H. Hanaor and C. C. Sorrell, *Adv. Eng. Mater.*, 2014, **16**, 248–254.
5 G. Jacobs, T. K. Das, Y. Zhang, J. Li, G. Racoillet and B. H. Davis, *Appl. Catal., A*, 2002, **233**, 263–281.
6 A. T. Bell, *Science*, 2003, **299**, 1688–1691.
7 C. Hernández Mejía, T. W. van Deelen and K. P. de Jong, *Nat. Commun.*, 2018, **9**, 1–8.
8 M. Mehrbod, M. Martinelli, A. G. Martino, D. C. Cronauer, A. Jeremy Kropf, C. L. Marshall and G. Jacobs, *Fuel*, 2019, **245**, 488–504.
9 T. W. van Deelen, C. Hernández Mejía and K. P. de Jong, *Nat. Catal.*, 2019, **2**, 955–970.
10 M. Wolf, E. K. Gibson, E. J. Olivier, J. H. Neethling, C. R. A. Catlow, N. Fischer and M. Claeys, *ACS Catal.*, 2019, **9**, 4902–4918.
11 M. Wolf, N. Fischer and M. Claeys, *Nat. Catal.*, 2020, **3**, 962–965.
12 M. Wolf, N. Fischer and M. Claeys, *Chem Catal.*, 2021, **1**, 1014–1041.
13 U. Diebold, *Surf. Sci. Rep.*, 2003, **48**, 53–229.
14 Q. Fu, T. Wagner, S. Olliges and H. D. Carstanjen, *J. Phys. Chem. B*, 2005, **109**, 944–951.
15 Q. Fu and T. Wagner, *Surf. Sci. Rep.*, 2007, **62**, 431–498.
16 V. A. de la Peña O'Shea, M. Consuelo Álvarez Galván, A. E. Platero Prats, J. M. Campos-Martin and J. L. G. Fierro, *Chem. Commun.*, 2011, **47**, 7131–7133.
17 N. N. Greenwood and A. Earnshaw, in *Chemistry of the Elements*, ed. N. N. Greenwood and A. Earnshaw, Elsevier Ltd., 2nd edn, 1997, vol. 92, pp. 954–975.
18 S. Bagheri, N. Muhd Julkapli and S. B. A. Hamid, *Sci. World J.*, 2014, **2014**, 1–21.

Open Access Article. Published on 24 February 2023. Downloaded on 10/30/2025 4:25:35 AM.
This article is licensed under a Creative Commons Attribution 3.0 Unported Licence.

19 J. Li and D. Xu, *Chem. Commun.*, 2010, **46**, 2301.
20 L. Chu, Z. Qin, J. Yang and X. Li, *Sci. Rep.*, 2015, **5**, 12143.
21 B. Jongsomjit, C. Sakdamnuson and P. Praserthdam, *Mater. Chem. Phys.*, 2005, **89**, 395–401.
22 B. Jongsomjit, T. Wongsalee and P. Praserthdam, *Mater. Chem. Phys.*, 2005, **92**, 572–577.
23 T. V. Choudhary and D. W. Goodman, *Catal. Today*, 2002, **77**, 65–78.
24 A. Mishra and R. Prasad, *Bull. Chem. React. Eng. Catal.*, 2011, **6**, 1–14.
25 P. Mars and D. W. van Krevelen, *Chem. Eng. Sci.*, 1954, **3**, 41–59.
26 L. Lukashuk, N. Yigit, R. Rameshan, E. Kolar, D. Teschner, M. Hävecker, A. Knop-Gericke, R. Schlögl, K. Föttinger and G. Rupprechter, *ACS Catal.*, 2018, **8**, 8630–8641.
27 L. Lukashuk, K. Föttinger, E. Kolar, C. Rameshan, D. Teschner, M. Hävecker, A. Knop-Gericke, N. Yigit, H. Li, E. McDermott, M. Stöger-Pollach and G. Rupprechter, *J. Catal.*, 2016, **344**, 1–15.
28 T. M. Nyathi, N. Fischer, A. P. E. York and M. Claeys, *Faraday Discuss.*, 2017, **197**, 269–285.
29 M. Khasu, T. Nyathi, D. J. Morgan, G. J. Hutchings, M. Claeys and N. Fischer, *Catal. Sci. Technol.*, 2017, **7**, 4806–4817.
30 T. M. Nyathi, N. Fischer, A. P. E. York, D. J. Morgan, G. J. Hutchings, E. K. Gibson, P. P. Wells, C. R. A. Catlow and M. Claeys, *ACS Catal.*, 2019, **9**, 7166–7178.
31 T. M. Nyathi, N. Fischer, A. P. E. York and M. Claeys, *ACS Catal.*, 2020, **10**, 11892–11911.
32 T. M. Nyathi, M. I. Fadlalla, N. Fischer, A. P. E. York, E. J. Olivier, E. K. Gibson, P. P. Wells and M. Claeys, *Appl. Catal., B*, 2021, **297**, 120450.
33 M. I. Fadlalla, T. M. Nyathi and M. Claeys, *Catalysts*, 2022, **12**, 118.
34 M. C. M. Claeys and N. F. Fischer, Sample Presentation Device for Radiation-Based Analytical Equipment, *US Pat.*, 8597598B2, 2013.
35 N. Fischer and M. Claeys, *Catal. Today*, 2016, **275**, 149–154.
36 N. Fischer and M. Claeys, *J. Phys. D: Appl. Phys.*, 2020, **53**, 293001.
37 M. C. M. Claeys, E. W. J. van Steen, J. L. Visagie and J. van de Loosdrecht, Magnetometer, *US Pat.*, 8773118B2, 2014.
38 P. Munnik, N. A. Krans, P. E. de Jongh and K. P. de Jong, *ACS Catal.*, 2014, **4**, 3219–3226.
39 V. Sechovský, in *Encyclopedia of Materials: Science and Technology*, ed. K. H. J. Buschow, R. W. Cahn, M. C. Flemings, B. Ilschner, E. J. Kramer, S. Mahajan and P. Veyssière, Elsevier Science Ltd, 2nd edn, 2001, pp. 5018–5032.
40 A. A. Coelho, *J. Appl. Crystallogr.*, 2003, **36**, 86–95.
41 C. Weidenthaler, *Nanoscale*, 2011, **3**, 792–810.
42 E. Marceau, X. Carrier, M. Che, O. Clause and C. Marcilly, in *Handbook of Heterogeneous Catalysis*, ed. G. Ertl, H. Knözinger, F. Schüth and J. Weitkamp, Wiley-VCH Verlag GmbH & Co. KGaA, Weinheim, Germany, 2008, pp. 467–484.
43 E. van Steen, M. Claeys, M. E. Dry, J. van de Loosdrecht, E. L. Viljoen and J. L. Visagie, *J. Phys. Chem. B*, 2005, **109**, 3575–3577.
44 N. Fischer, E. van Steen and M. Claeys, *Catal. Today*, 2011, **171**, 174–179.
45 N. Fischer, M. Minnermann, M. Baeumer, E. van Steen and M. Claeys, *Catal. Lett.*, 2012, **142**, 830–837.
46 W. A. Sławiński, E. Zacharaki, H. Fjellvåg and A. O. Sjåstad, *Cryst. Growth Des.*, 2018, **18**, 2316–2325.
47 E. Klugmann, H. J. Blythe and F. Walz, *Phys. Status Solidi A*, 1994, **146**, 803–813.
48 S. Ram, *Mater. Sci. Eng., A*, 2001, **304–306**, 923–927.
49 H. E. du Plessis, J. P. R. de Villiers, A. Tuling and E. J. Olivier, *Phys. Chem. Chem. Phys.*, 2016, **18**, 30183–30188.
50 E. van Steen, G. S. Sewell, R. A. Makhothe, C. Micklethwaite, H. Manstein, M. de Lange and C. T. O'Connor, *J. Catal.*, 1996, **162**, 220–229.
51 L. Zhong, T. Kropp, W. Baaziz, O. Ersen, D. Teschner, R. Schlögl, M. Mavrikakis and S. Zafeiratos, *ACS Catal.*, 2019, **9**, 8325–8336.
52 L. Zhong, M. Barreau, V. Caps, V. Papaefthimiou, M. Haevecker, D. Teschner, W. Baaziz, E. Borfecchia, L. Braglia and S. Zafeiratos, *ACS Catal.*, 2021, **11**, 5369–5385.
53 L. Zhong, M. Barreau, D. Chen, V. Caps, M. Haevecker, D. Teschner, D. H. Simonne, E. Borfecchia, W. Baaziz, B. Šmíd and S. Zafeiratos, *Appl. Catal., B*, 2021, **297**, 120397.
54 R. C. Reuel and C. H. Bartholomew, *J. Catal.*, 1984, **85**, 78–88.
55 R. E. Newnham, J. H. Fang and R. P. Santoro, *Acta Crystallogr.*, 1964, **17**, 240–242.
56 M. Wolf, N. Fischer and M. Claeys, *Mater. Chem. Phys.*, 2018, **213**, 305–312.
57 M. Wolf, S. J. Roberts, W. Marquart, E. J. Olivier, N. T. J. Luchters, E. K. Gibson, C. R. A. Catlow, J. H. Neethling, N. Fischer and M. Claeys, *Dalton Trans.*, 2019, **48**, 13858–13868.
58 A. J. Dent, G. Cibin, S. Ramos, A. D. Smith, S. M. Scott, L. Varandas, M. R. Pearson, N. A. Krumpa, C. P. Jones and P. E. Robbins, *J. Phys.: Conf. Ser.*, 2009, **190**, 012039.

 This journal is © The Royal Society of Chemistry 2023